



Modeling and optimal design of multicomponent vacuum pressure swing adsorber for simultaneous separation of carbon dioxide and hydrogen from industrial waste gas

Toji Kakiuchi¹ · Tomoyuki Yajima¹ · Nobuyuki Shigaki² · Yoshiaki Kawajiri¹

Received: 30 March 2022 / Revised: 20 July 2022 / Accepted: 1 November 2022 / Published online: 22 November 2022
© The Author(s), under exclusive licence to Springer Science+Business Media, LLC, part of Springer Nature 2022

Abstract

Adsorption processes are expected to play an important role in carbon dioxide capture, utilization and storage (CCUS). In particular, blast furnace gas (BFG) from the steel industry is one of the major sources of CO₂ emissions, and reducing emissions from this source is a major challenge. BFG can be treated as valuable hydrogen (H₂) source through water gas shift reactions, which may allow synthesis of methane and methanol if the purification of these two gases is possible. This study proposes and designs a new Vacuum Pressure Swing Adsorption (VPSA) process that consists of two tandem adsorption columns for simultaneous separation of H₂ and CO₂ from BFG. A mathematical model is developed to predict the performance of the proposed process. The model is fitted to the experimental data using a VPSA pilot plant, which were demonstrated to predict flow rates within an error of 6%. Furthermore, the model was used to perform multi-objective optimization to analyze trade-offs among throughput, energy consumption, CO₂ purity, and recovery. Finally, we analyzed the optimal design and operating conditions such as pressure and column height.

Keywords Vacuum pressure swing adsorption · CO₂ capture · Multicomponent separation · Optimal design

List of symbols

ad_{ratio}	Ratio of adsorption time to desorption time [–]	F	Feed inflow rate [NL/min]
C	Total concentration [mol/m ³]	F_{in}	Feed gas flow rate [NL/min]
C_i	Concentration of component i [mol/m ³]	$Flow$	Flow rate from the column [NL/min]
Cp_g	Heat capacity of gas [J/kg/K]	h_{air}	Heat transfer coefficient of air [J/m ² /s/K]
Cp_s	Heat capacity of solid [J/kg/K]	h_i	Heat transfer coefficient [J/m ² /s/K]
Cp_w	Wall heat capacity [J/kg/K]	K_i	Affinity constant of component i [bar ⁻¹]
De	Effective diffusivity [m ² /s]	K_L	Effective axial thermal coefficient [J/m/s/K]
$D_{i,j}$	Gas diffusivity [m ² /s]	L_1, L_2	Height of column 1 and 2 [m]
D_p	Adsorbent diameter [m]	M	Penalty constant
D_X	Axial dispersion coefficient [m ² /s]	Mw_i	Molecular weight of component i [g/mol]
D_z	Dispersion coefficient [m ² /s]	N_{Comp}	Number of components
E	Energy consumption for a unit mole of recovered gas [kJ/mol]	P	Total pressure [Pa]
E_{max}	Upper bound of energy consumption [kJ/mol]	P_1, P_2	Pressure of column 1 and column 2 [kPa]
$Feed$	Total molar volume of gas that enters the VPSA [mol/m ²]	P_{atm}	Atmospheric pressure [kPa]
		P_i	Partial pressure of component i [bar]
		P_{in}	Pressure of column inlet [Pa]
		Pur_{min}	Lower bound of purity [%]
		q_{oi}	Saturation capacity [mol/kg]
		q_i	Adsorption amount of component i [mol/kg]
		q_i^*	Adsorption amount of component i in the equilibrium state [mol/kg]
		R	Gas constant [J/k/mol]
		R_b	Radius of the column [m]
		Rec_{min}	Lower bound of recovery [%]

✉ Yoshiaki Kawajiri
kawajiri@nagoya-u.jp

¹ Department of Materials Process Engineering, Nagoya University, Nagoya 464-8603, Japan

² Steel Research Laboratory, JFE Steel Corporation, 1 Kokan-Cho, Fukuyama, Japan

Re_p	Particle Reynolds number [–]
R_p	Adsorbent radius [m]
Si	Set for step index [–]
t	Time [s]
T_{air}	Air temperature [K]
t_{cy}	Cycle time [t]
T_{in}	Temperature of column inlet [K]
T_{wall}	Wall temperature [K]
u	Superficial velocity [m/s]
U	Overall heat transfer coefficient [J/m/s/K]
$work_{ad}$	Work of adsorption [kJ]
$work_{de}$	Work of desorption [kJ]
y_i	Mole fraction of component i [–]
z	Coordinate in the axial direction [m]

Greek letters

α, β	Parameters for approximation of pressure
γ	Heat capacity ratio [–]
γ_i, δ_i	Parameters used in the boundary conditions
ΔH_i	Adsorption enthalpy [J/mol]
$\varepsilon_1, \varepsilon_2$	Tolerance variables to enforce a cyclic steady state for column 1 and 2 [–]
ε_b	Bed void [–]
ε_t	Total void fraction [–]
η_{blower}	Efficiency of blower [–]
η_{pump}	Efficiency of pump [–]
θ	Vector of parameters to be estimated
θ_{lit}	Initial parameter value
λ_{ads}	Thermal conductivity of solid [J/m/s/K]
λ_g	Estimated thermal conductivity of gas [J/m/s/K]
λ_{wall}	Thermal conductivity of wall [J/m/s/K]
μ	Viscosity [Pa s]
ρ	Regularization coefficient [–]
ρ_b	Density of bed [kg/m ³]
ρ_g	Density of gas [kg/m ³]
ρ_p	Adsorbent density [kg/m ³]
ρ_w	Wall density [kg/m ³]
φ	Vector of state variables

Subscripts

ad	Adsorption
bl	Blowdown
de	Desorption
exp	Experimental value
lit	Literature value
$Model$	Modeled value
pr	Pressurization

1 Introduction

The rising concentration of carbon dioxide (CO₂) in the atmosphere is posing a severe threat to the global climate [1, 2]. For this problem, carbon dioxide capture, storage, and utilization (CCUS) has attracted attention [3], which

is a technological concept to capture CO₂ from various sources, and pump it into the ground and seawater or use it as a resource. It is estimated that CCUS could reduce 20% of worldwide CO₂ emissions in 2008 [4]. In particular, blast furnace gas in the steel industry is one of the significant sources of CO₂ emissions [5, 6], and application of CCUS technologies to this source is expected [7].

In the steel industry, a large amount of CO₂ is released to the atmosphere from blast furnaces. Blast furnace gas (BFG), generated in furnaces when iron is produced from iron ore and coke, mainly consists of CO₂, nitrogen (N₂) and carbon monoxide (CO), as well as a small amount of hydrogen (H₂). The CO in BFG can be converted into CO₂ and H₂ by steam reforming. The H₂ produced through steam reforming in addition to that exists originally in BFG, can be utilized as a hydrogen source for CCUS. Furthermore, the concentration of CO₂ in the BFG increases by steam reforming, which facilitates the CO₂ separation [8, 9]. Methane and methanol, promising products of CO₂ utilization in CCUS, can be produced from CO₂ and H₂ that exist in the reformed BFG [10, 11]. The H₂ must be separated from CO₂ and impurities [12]. Thus, simultaneous recovery of CO₂ and H₂ from BFG after reforming preferably by a single separation unit is expected to realize the proposed CCUS approach. Here, it is assumed that the BFG is withdrawn partially, but not totally from a furnace.

A promising technique for capturing CO₂ is Pressure Swing Adsorption (PSA), or Vacuum Pressure Swing Adsorption (VPSA) [13, 14]. This separation technique has been used in many applications of large-scale gas separation [15–17]. However, power consumption and energy cost must be reduced substantially for successful CCUS implementation [17, 18]. A study reported that the estimated cost is \$72–114 per ton of CO₂ for capture and storage, most of which is spent to capture CO₂ [19]. It is expected that this cost should be reduced to approximately \$18 [17]. To reduce the compression and transportation cost, concentrating CO₂ efficiently is critical [20, 19].

PSA and VPSA are often used to enrich weakly adsorbed components such as H₂, and most of the conventional designs are found to be ineffective for purifying strongly adsorbed components [21–23] such as CO₂. Indeed, a past simulation study of classical PSA showed that when the CO₂ recovery is increased, the purity of the recovered gas is only about 50% [24]. Various operating methods have been proposed and verified to overcome these shortcomings, one of which is the pressure equalization step. Ho et al. reported that by introducing the pressure equalization step, the purity of the recovered gas is around 90%, which is almost 50% higher than classical PSA [25]. In addition, Xiao et al. reported that the purity and recovery rate were more than 90% by introducing the pressure equalization step twice [26]. On the other hand,

a pressure equalization step has disadvantages such as increased equipment cost and complicated operations [27]. An alternative approach to pressure equalization is rinse, which supplies high-purity CO₂ gas into the column before desorption [27] to displace impurities. Choi et al. reported that the purity could increase to 90% by introducing the rinse step and the pressure equalization step [28]. On the other hand, one of the problems of the rinse step is that the recovery tends to decrease because the captured gas is re-injected into the column [27]. To overcome this problem, a method has been proposed in which the gas discharged during the rinse step is recycled into the column during the adsorption step [29].

It is also known that the design and operating conditions of VPSA must be determined carefully to optimize the performance. For example, Kim et al. reported the purity and recovery of recovered gas varied significantly with the choice of desorption and adsorption pressures [30]. In particular, changing the pressure during desorption by a few kPa in VSA can significantly reduce both the purity and the recovery [31]. In addition, some studies have also investigated the effects of changes in cycle time, inflow rate, etc., indicating the importance of determining operating conditions [32–34, 26].

In addition, purifying multiple gas species simultaneously using a single adsorption unit remains a challenge. Air Products and Chemicals, Inc. designed multiple PSA units for CO₂ and ammonia synthesis gas separation [35]. Dong et al. also proposed a PSA for separating CO₂, CH₄, and N₂ using three types of adsorbents and multiple adsorption columns [36]. While high purity and recovery can be achieved in these methods, multiple units are needed, which may increase the capital cost. In addition, these processes require a large number of columns, pumps and compressors [37–39]. The complexity of such processes would not allow easy analysis and optimization [35], and may pose operational challenges.

Another problem with VPSA for simultaneous separation of CO₂ and H₂ is the low concentration of H₂ in the feed gas. In past studies, the H₂ concentration in the feed gas has been higher than 50%, while the H₂ concentration in the reformed BFG is as low as 25%. To the best of our knowledge, sufficient effort has not been made for H₂ purification from dilute H₂ sources, which is a bottleneck for separating CO₂ and H₂ simultaneously from BFG [40].

In this study, a new adsorption process for simultaneous separation of H₂ and CO₂ from steam reformed BFG is proposed, and its performance is verified using a laboratory-scale system. The proposed process achieves high CO₂ purity and recovery and simultaneous recovery of H₂ from the dilute hydrogen source by fractionation downstream of the column. The reformed BFG can be supplied continuously to the proposed process without a buffer tank by using

only two columns, which is a substantial decrease of capital cost compared to conventional approaches that require at least four columns. Furthermore, there is no rinse or pressure equalization step, eliminating the need for extra energy and capital cost for blower or compressor. This process was analyzed using a mathematical model to estimate concentration and temperature profiles which cannot be measured experimentally. In our model, the adsorption isotherm parameters are refined using the experimental data from the VPSA pilot plant employing Tikhonov regularization to suppressing overfitting. Using the developed model, multi-objective optimization of energy consumption and throughput was performed, which identified potential improvement from our experimental investigations. We further analyzed the relationship among multiple performance indicators, including purity, recovery, energy consumption and throughput, finding the optimal operating conditions and design.

The structure of the paper is as follows. Section 2 describes the proposed process and experimental setup for simultaneous separation. The developed model, parameters, boundary conditions, model fitting, and optimization methods are presented in Sect. 3. In Sect. 4, we first present the fitting results and confirm the accuracy by comparing them with experimental results. The results of the optimization under two different conditions were then presented. In the first case, we compared the results with the experimental results and confirmed potential improvement. Finally, the performance and operating conditions were analyzed.

2 Process description

2.1 Principles of proposed process

The new VPSA process proposed in this study exploits the differences in isotherm shapes among adsorbates [41]. In Fig. 1a, isotherms of two components CO₂ and N₂, are shown. The isotherm of N₂, which adsorbs to the adsorbent weakly, is nearly linear with respect to pressure, as shown in Fig. 1a. On the other hand, the isotherm of CO₂, which adsorbs to the adsorbent strongly, is concave. Because of the differences, the selectivity of the two components depends on the pressure: the selectivity in the period from (2) to (3), $m_{\text{CO}_2(2)-(3)}/m_{\text{N}_2(2)-(3)}$, is higher than that in the period from (1) to (2), $m_{\text{CO}_2(1)-(2)}/m_{\text{N}_2(1)-(2)}$.

The dependence of the selectivity on the pressure determines the concentration profiles of the product stream, which is withdrawn by the vacuum operation of VPSA processes. Separation of components in the process is determined by the driving force, which is the difference between the amount adsorbed in the adsorbent and the equilibrium capacity. In the vacuum operation where desorbed gas continues to be released from the adsorbent, the total pressure

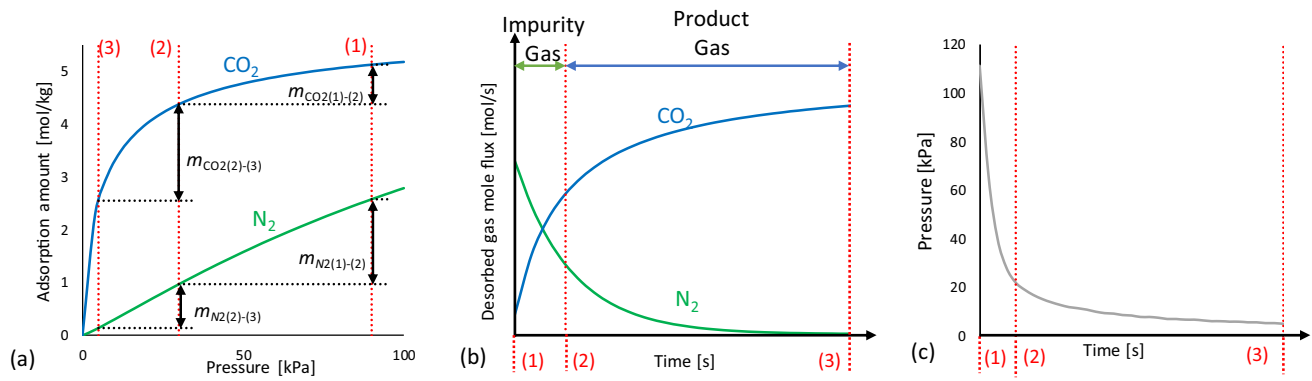


Fig. 1 Principles of proposed VPSA: **a** isotherms for two different adsorbates **b** illustration of molar flowrate profiles during desorption step **c** illustration of pressure profile during desorption step

cannot always be decreased instantaneously but at a finite rate, and thus the selectivity changes as the vacuum operation continues. Thus, the total pressure changes as shown in Fig. 1b, and the selectivity changes accordingly from (1) to (3). In Fig. 1c, only N₂ is desorbed at the beginning (1), but as the total pressure continues to be decreased to (2) and (3), the concentration of CO₂ increases more rapidly compared to N₂. This principle has been applied to separation of CO₂ using a single column by Shigaki et al. [41], and this study extend this approach to multi-component separation for the first time.

The time dependence of the selectivity illustrated above allows purification of components by fractionation at the outlet off the column. As shown in Fig. 1c, the outflowing gas from the column in the duration between (1) and (2) is collected as “Impurity”, and that between (2) and (3) is collected as “Product gas” (Fig. 1b). More specific examples of such operations are discussed below.

2.2 Multicomponent separation by fractionation

Figure 2 shows the operation of the proposed VPSA for multi-component gas separation for CO₂ and H₂ in reformed BFG from a water gas shift reactor. The process consists of two tandem columns, which allow the separation of two gas components within one cycle without excessive energy penalty, as discussed more in detail in Sect. 4.2.2. In this operation, one cycle consists of six operation steps. In the pressurization step, the pressure inside the column is increased. In the following adsorption step, CO₂, the component with the highest affinity toward the adsorbent, is captured in column 1. Simultaneously in this step, N₂, the component with the second-highest affinity, is adsorbed in column 2. As these two components are captured, H₂, the component with the lowest affinity toward the adsorbent, is concentrated in the gas phase and collected at the outlet of column 2. In the following blowdown process, the pressure in the column is decreased to the target pressure by discharging the internal

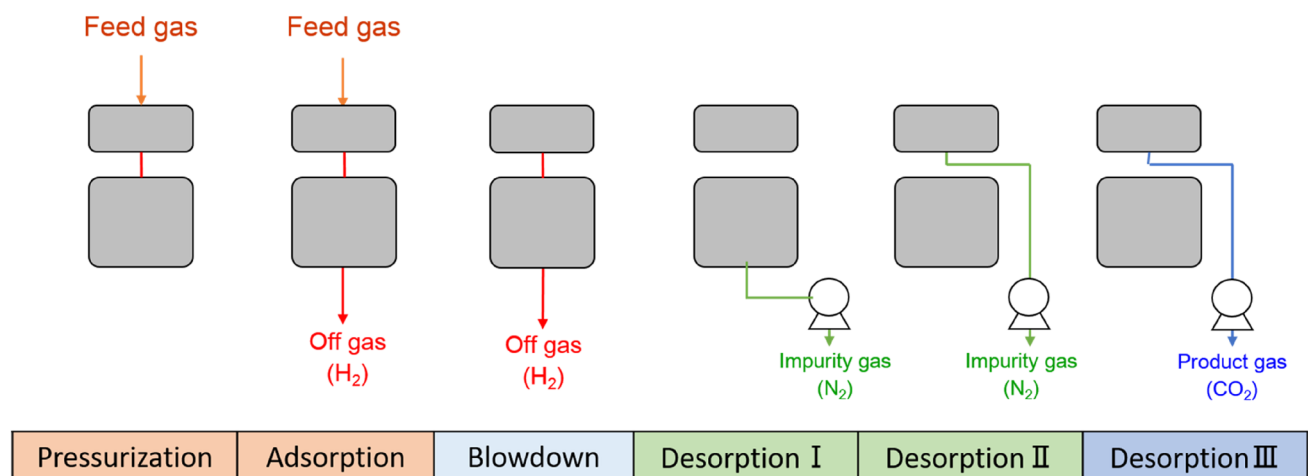


Fig. 2 Operation of VPSA for multiple separations

gas through the backpressure valve. In the following step, desorption I, column 2 is depressurized using a vacuum pump to regenerate the adsorbent in column 2. Then, in desorption II and III, column 1 is depressurized using a vacuum pump to regenerate the adsorbent in column 1. At this time, N₂-rich gas flows out immediately, and CO₂-rich gas flows out subsequently as the depressurization operation continues. In these three-step desorption operation, the purity of CO₂ is increased by discharging N₂-rich gas as Impurity gas and collecting CO₂-rich gas as Product gas.

There are three unique aspects in this process. The first is that the column is split into two, which have different roles. As mentioned above, the first column captures CO₂ from the feed gas, while the second column purifies H₂ in the outflow gas from column 1. The second aspect is rinse or pressure equalization operations are not employed while maintaining high purity and recovery, which is accomplished by utilizing the gas fraction line and the difference in adsorption strength between N₂ and CO₂, as explained in Sect. 2.1. The absence of rinse and pressure equalization steps eliminates the need for equipment to introduce rinse gas and additional columns, allowing continuous supply of the feed gas only with two columns eliminating equipment complexity and cost increase. The third is that the gas flow is always in one direction. As can be seen from Fig. 2, the inlet line of the feed gas and the outlet line of the desorbed gas are located on opposite sides of the two columns. This design avoids contamination of the product gas by impure species in the feed gas, which would occur in the conventional designs where supply of feed gas and withdrawal of the product gas are performed on the same side sharing the same line.

2.3 Experimental method

To verify the performance of the CO₂-H₂ simultaneous separation VPSA, laboratory-scale VPSA experiments were conducted using the experimental setup shown in Fig. 3. Table 1 also shows the experimental conditions of the VPSA process. The feed gas is supplied from the top of the adsorption column as a mixture consisting of N₂, CO₂, and H₂. The constituent gases are prepared using gas cylinders, which have a purity of 99.99% or higher. Mass flow controllers control the feed gas composition, which mix the gases in the ratio shown in Table 1, and supply them at a constant flow rate. The cylindrical adsorption columns are made of stainless steel and have an inner diameter of 43 mm. The height of column 1 is 60 mm, and column 2 is 200 mm. Zeolite 13X pellets with a diameter of 1.5 mm were used as the adsorbent. Column 1 was packed with 57 g and column 2 with 190 g of the zeolite. Two gas channels are placed downstream of column 1 lead to column 2 and the vacuum pump for desorption. The downstream side of column 2 has three gas channels, two of which are for Off Gas connected to back pressure valves, and another for Impurity and Product to a vacuum pump. A valve is installed downstream of the vacuum pump to realize gas fraction. The gas channel was changed by an automatic valve operated by compressed air, and the timing for opening and closing the valve was decided in advance. The adsorption pressure was adjusted by a back pressure valve attached to the outlet lines for Off Gas. The target desorption pressure to be reached at the end of the desorption step was adjusted by a needle valve upstream of the vacuum pump. The gas volume was measured with an

Fig. 3 Experimental setup

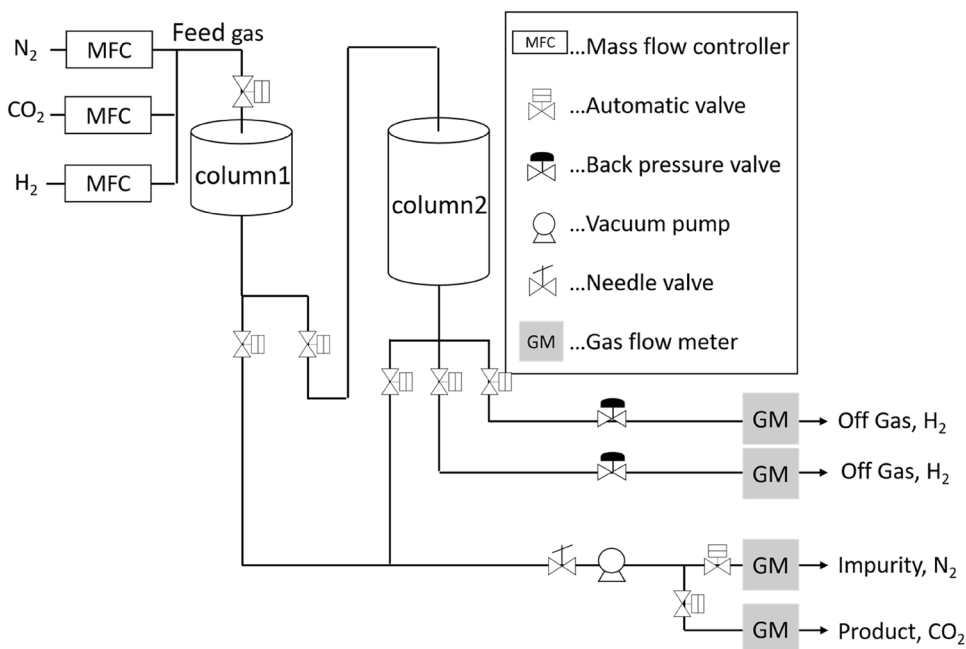


Table 1 Experimental condition

Condition	Value	Condition	Value
Adsorbent	Zeolite13X	Feed gas composition [%]	N ₂ :40,CO ₂ :37 H ₂ :23
Pellet diameter [mm]	1.5	Feed gas temperature [K]	298.15
Height of column [mm]	Column 1:60 Column 2:200	Cycle time [s/cycle]	80,90,100,110
Weight of adsorbent [g]	Upper:57 Lower:190	Pressure at the bottom of column [kPaG]	Adsorption: 50 Desorption: -95
Column inner diameter [mm]	43	Feed gas flow rate [NL/min]	3.0
Blowdown pressure [kPa]	101	Desorption pressure [kPa]	3.0–5.1

integrated gas flow meter installed at each gas outlet. The temperature inside the column was not measured due to the difficulty in placing a thermocouple.

3 Method

3.1 Mathematical model

A model was developed under the following assumptions [38, 39].

- (1) The gas in the column follows the ideal gas law.
- (2) The radial variations of temperature and concentration can be ignored.
- (3) The temperature dependence of viscosity, thermal conductivity, and diffusion coefficient is negligible.
- (4) The adsorbent and gas are in thermal equilibrium and at the same temperature.
- (5) Competitive adsorption follows the Langmuir equation.
- (6) Mass transfer rate across the gas and adsorbent phases is given by the LDF model.

The overall mass balance equation is given by

$$\frac{\partial C}{\partial t} - D_z \frac{\partial^2 C}{\partial z^2} + \frac{\partial(uC)}{\partial z} + \rho_p \frac{1 - \varepsilon_b}{\varepsilon_b} \sum \frac{\partial q_i}{\partial t} = 0 \quad (1)$$

where C [mol/m³] is the total concentration; t [s] is the time; D_z [m²/s] is the dispersion coefficient; u [m/s] is the superficial velocity; ρ_p [kg/m³] is the adsorbent density; ε_b [–] is the bed void; q_i is the adsorption amount of component i ; subscripts i is for the gas component. Here, the equation of state for an ideal gas is given by

$$C = \frac{P}{RT} \quad (2)$$

where P [Pa] is the total pressure; and R [J/k/mol] is the gas constant. In the target process, the flow velocity in the axial direction of the column is not constant due to density change caused by pressure change and adsorption/desorption

of each component. The total concentration balance equation is implemented in the model in order to calculate the flow velocity considering the pressure change and adsorption/desorption.

The mass balance equation of each component is given by

$$\frac{\partial C_i}{\partial t} - D_z \frac{\partial^2 C_i}{\partial z^2} + \frac{1}{\varepsilon_b} \frac{\partial(uC_i)}{\partial z} + \rho_p \frac{1 - \varepsilon_b}{\varepsilon_b} \frac{\partial q_i}{\partial t} = 0 \quad (3)$$

where C_i [mol/m³] is the concentration of component i . Summing this equation for all component i gives Eq. (1) with $C = \sum_i C_i$. Since C_i is the product of the total concentration C and the mole fraction y_i [–].

The energy balance for the column is given by

$$\begin{aligned} (\varepsilon_t \rho_g C_{p_g} + \varepsilon_b \rho_b C_{p_s}) \frac{\partial T}{\partial t} + \rho_g C_{p_g} u \frac{\partial T}{\partial z} - K_L \frac{\partial^2 T}{\partial z^2} \\ - \rho_b \sum \Delta H_i \frac{\partial q_i}{\partial t} + 2 \frac{h_i}{R_b} (T - T_{wall}) = 0 \end{aligned} \quad (4)$$

where ε_t [–] is the total void fraction; ρ_b and ρ_g [kg/m³] are the density of bed and gas, respectively; C_{p_g} and C_{p_s} [J/kg/K] are the heat capacity of gas and solid; K_L [J/m/s/K] is the effective axial thermal coefficient; ΔH_i [J/mol] is adsorption enthalpy; h_i [J/m²/s/K] is the heat transfer coefficient; R_b [m] is the radius of the column; and T_{wall} [K] is the wall temperature. It should be noted that in the above equation involves many assumptions, such as constant heat of adsorption ΔH_i , ignoring heat loss to the environment, and constant bed density ρ_b . Further details can be found in Ko et al. [42], Ko et al. [43], Ribeiro et al. [44], and Luberti et al. [45].

The energy balance for the column wall is given by

$$\rho_w C_{p_w} (R_o^2 - R_b^2) \frac{\partial T_{wall}}{\partial t} = 2\pi R_b h_i (T - T_{wall}) - 2\pi U (T_{wall} - T_{air}) \quad (5)$$

where, ρ_w [kg/m³] is the wall density; C_{p_w} [J/kg/K] is the wall heat capacity; U [J/m/s/K] is the overall heat transfer coefficient; T_{air} [K] is the air temperature.

The pressure drop can be described by Ergun's equation

$$\frac{\partial P}{\partial z} = -\frac{150\mu}{Dp^2} \frac{(1 - \epsilon_b)^2}{\epsilon_b^3} u - \frac{1.75\rho_g}{Dp} \frac{1 - \epsilon_b}{\epsilon_b^3} |u|u \tag{6}$$

where, D_p [m] is the adsorbent diameter; μ [Pa s] is the viscosity.

Mass transfer rate across the gas and adsorbent phases can be represented by the LDF model

$$\frac{\partial q_i}{\partial t} = \frac{15De}{Rp^2} (q_i^* - q_i) \tag{7}$$

where De [m²/s] is the effective diffusivity; R_p [m] is the adsorbent radius; q_i^* [mol/kg] is the adsorption amount of component i in the equilibrium state. Here, q_i^* is given by the competitive Langmuir isotherm

$$q_i^* = \frac{q_{0i}K_iP_i}{1 + \sum K_iP_i} \tag{8}$$

$$K_i = K_{1i} \exp\left(1000K_{2i}\left(\frac{1}{T} - \frac{1}{T_{ref}}\right)\right) \tag{9}$$

where, q_{0i} [mol/kg] is the saturation capacity; K_i [bar⁻¹] is the affinity constant; and P_i [bar] is the partial pressure of component i . The reference temperature T_{ref} is set to 250 K. This low temperature was chosen to avoid potential numerical difficulties; by setting this temperature to be sufficiently low, the sign of $(1/T - 1/T_{ref})$ always remains negative.

The gas density and the inflow rate of the feed gas are given by the following equations.

$$\rho_g = \frac{P \sum M_{w_i}y_i}{1000RT} \tag{10}$$

$$u_f = \frac{F_{in}}{60 \times 1000} \frac{1.01 \times 10^5 T_{in}}{273.15} \frac{1}{P_{in} R_b^2 \pi} \tag{11}$$

where M_{w_i} [g/mol] is the molecular weight of component i ; F_{in} [NL/min] is the feed gas flow rate, T_{in} [K] is the temperature of column inlet; and P_{in} [Pa] is the pressure of column inlet.

3.2 Boundary conditions and parameters

Boundary conditions for each step were set referring to previous studies [42, 43]. The parameters used in the model are shown in Table 2. Boundary conditions except for outlet pressure are shown in Table S2 and Table S3. In this study, there is a time-dependent fractional flow operation, and thus modeling the gas flow rate is critical. To reproduce the gas flow rate, the profiles of pressurization and depressurization with respect to time should also be

accurately modeled, and the outlet pressure were set to be follow the experimental results.

The boundary conditions of column outlet pressure for the simulation are given as polynomials up to the third-order in each of nine sections in a cycle:

$$P_1|_{z=L_1} = \alpha_{i,3}t^3 + \alpha_{i,2}t^2 + \alpha_{i,1}t + \alpha_{i,0} \quad t_{i-1} \leq t \leq t_i, \quad i = 1, 2, \dots, 9 \tag{12}$$

$$P_2|_{z=L_2} = \beta_{i,3}t^3 + \beta_{i,2}t^2 + \beta_{i,1}t + \beta_{i,0} \quad t_{i-1} \leq t \leq t_i, \quad i = 1, 2, \dots, 9 \tag{13}$$

where P_1 and P_2 [kPa] are the pressure of column 1 and column 2, respectively; L_1 and L_2 [m] are the height of column 1 and 2. Here, t is the elapsed time from the start of each section, and the time intervals are given as follows: $t_0 = 0$ and $t_i = \{3, 30, 50, 51, 55, 65, 67, 70, 100\}$. The constants in the equations were determined from the experimental pressure measurement. The results of the fitting will be presented in Sect. 4.

The physical properties of the adsorbent porosity and density were obtained by measuring the weight and volume before and after the column was permeated with water. Among the parameters listed in Table 2, K_L , U , h_i , and D_x are estimated as follows: the Effective axial thermal coefficient, K_L [J/m/s/K] is estimated using the following equations [47].

$$\lambda^{e0} = \lambda_g \epsilon_b + \frac{1 - \epsilon_b}{0.22 \frac{\epsilon_b^2}{\lambda_g} + \frac{2\lambda_{ads}}{3}} \tag{14}$$

$$K_L = \lambda^{e0} + 0.5D_p u C p_g \rho_g \tag{15}$$

where λ_{ads} [J/m/s/K] is the thermal conductivity of solid, and λ_g is that of gas estimated as a weighted average by compositions.

The overall heat transfer coefficient U [J/m/s/K] is estimated by the following equation.

$$U = \left(\frac{1}{R_o h_{air}} + \frac{1}{\lambda_{wall}} \ln \frac{R_o}{R_b} \right)^{-1} \tag{16}$$

where λ_{wall} [J/m/s/K] is the thermal conductivity of wall; h_{air} [J/m²/s/K] is the heat transfer coefficient of air. The heat transfer coefficient for component i , h_i [J/m²/I/K], is estimated by the following equations [48].

$$Nu_w = 4.21 Re_p^{0.365} \tag{17}$$

$$Nu_w = \frac{h_i R_b}{\lambda_g} \tag{18}$$

where, Re_p [-] is the particle Reynolds number.

Table 2 Model parameters

Parameter	Value	Unit	
ρ_p	Adsorbent density	1580	kg/m ³ Shigaki et al. [7]
ε_b	Bed void	0.57	– This study
ε_t	Total void fraction	0.746	– This study
ρ_b	Bed density	670	kg/m ³ Shigaki et al. [7]
Cp_s	Heat capacity of the solid	1340	J/kg/K This study
K_L	Effective axial thermal coefficient	0.43	J/m/s/K Equation (17)
h_i	Heat transfer coefficient	18.2	J/m ² /s/K Equation (20)
R_b	Column radius	0.0215	m This study
ρ_w	Wall density	7930	kg/m ³ Stainless Steel Association [46]
Cp_w	Heat capacity of the wall	500	J/kg/K Stainless Steel Association [46]
R_o	Column outside radius	2.43×10^{-2}	m This study
U	Overall heat transfer coefficient	0.266	J/m/s/K Equation (18)
μ	Viscosity	1.45×10^{-5}	Pa × s Kagaku Kogakukai ed. [47]
λ_{ads}	Thermal conductivity of adsorbent	0.3	J/m/s/K Shigaki et al. [41]
λ_{wall}	Thermal conductivity of wall	16	J/m/s/K Stainless Steel Association [46]
h_{air}	Heat transfer coefficient of air	11	J/m ² /s/K Kagaku Kogakukai ed.[47]
R_p	Adsorbent radius	7.50×10^{-4}	m Shigaki et al. [7]
D_x	Diffusivity coefficient of N ₂	4.36×10^{-5}	m ² /s Kagaku Kogakukai ed. [47]
	Diffusivity coefficient of CO ₂	4.40×10^{-5}	m ² /s Kagaku Kogakukai ed. [47]
	Diffusivity coefficient of H ₂	6.44×10^{-5}	m ² /s Kagaku Kogakukai ed. [47]
λ_g	Thermal conductivity of N ₂	2.41×10^{-2}	W/m/K Kagaku Kogakukai ed. [47]
	Thermal conductivity of CO ₂	1.45×10^{-2}	W/m/K Kagaku Kogakukai ed. [47]
	Thermal conductivity of H ₂	1.68×10^{-1}	W/m/K Kagaku Kogakukai ed. [47]
$D_{i,j}$	Gas diffusivity between N ₂ and CO ₂	1.44×10^{-5}	m ² /s Kagaku Kogakukai ed. [47]
	Gas diffusivity between N ₂ and H ₂	6.66×10^{-5}	m ² /s Kagaku Kogakukai ed. [47]
	Gas diffusivity between H ₂ and CO ₂	5.52×10^{-5}	m ² /s Kagaku Kogakukai ed. [47]

The axial dispersion coefficient D_X [m²/s] is estimated by the following equations [49].

$$D_{m,i} = \frac{1 - y_i}{\sum_i \frac{y_i}{D_{i,j}}} \quad (19)$$

$$D_{z,i} = 0.73D_{m,i} + \frac{uR_p/\varepsilon_b}{1 + 9.49 \frac{\varepsilon D_{m,i}}{2uR_p}} \quad (20)$$

where $D_{i,j}$ [m²/s] is the gas diffusivity as listed in Table 2. The values at the inlet of column 1 at the end of the adsorption process were used as representative values for flow rate, mole fraction, gas density, and heat capacity of the gas.

3.3 Model fitting

To improve the prediction accuracy of the VPSA model, fitting to the experimental results was performed. A conventional approach to improve the prediction accuracy is to develop an accurate adsorption isotherm model from isotherm measurement data. However, the VPSA in this study

is a three-component system, which requires a large number of isotherm measurement points to quantify interactions among the components. In general, experiments to measure the amount of adsorption are time-consuming. Estimation even with the data from the past laboratory study using the same adsorbent does not necessarily assure that the isotherm has been modeled sufficiently accurately.

In this study, we propose an approach where the experimental data from the pilot plant test are *utilized together* with the laboratory isotherm measurements. Such an approach is made possible by Tikhonov regularization where the two different experimental data sets are considered simultaneously. This approach has been demonstrated in previous studies for liquid-phase adsorption processes [50–52]. In this approach, the model parameters were estimated using the following equation as the objective function.

$$\min_{\theta} \sum_{j=1}^3 \sum_{i=1}^{N_{Comp}} (Flow_{i,j,Model} - Flow_{i,j,exp})^2 + \rho \sum_{i=1}^{N_{Comp}} \left(\frac{\theta_i - \theta_{lit,i}}{\theta_{lit,i}} \right)^2 \quad (21)$$

where N_{Comp} is the number of components, with $N_{Comp} = 3$; θ is the vector of parameters to be estimated; $Flow$ [NL/min]

is the flow rate from the column; $\rho [-]$ is the regularization coefficient; subscripts j is for steps shown in Fig. 1; *Model* and *exp* denote modeled and experimental value, and subscript *lit* denotes the literature parameter value. The parameter vector θ is defined as $\theta = [K_1, K_2, De]^T$. In this study, we do not estimate the saturation capacity q_{0i} but fix them to the original values, since they are highly correlated to K_1 and K_2 which lead to failure in estimation.

The objective function, Eq. (21), consists of two terms with different roles. The first term is the sum of the errors between the values given by the modeled and experimental results. The second term is for the Tikhonov regularization, which acts as a penalty in the fitting. The minimization of this term prevents the estimated value from deviating significantly from the initial parameter value $\theta_{lit,i}$. In addition, ρ is the regularization factor, as mentioned earlier, balancing the two terms; if ρ was too large, the estimated value would converge around the initial value, and the error would not be reduced. In contrast, if ρ was too small, the fitting of the model would improve, the parameters would deviate significantly from the literature value $\theta_{lit,i}$, and thus the reliability of the parameters, as well as predictability of the model for unexperimented operating conditions would be diminished. In this study, we determine the value using multiple experimental data sets, as shown in Sect. 4.1.

3.4 Process optimization

There is a trade-off between the amount of gas processed and energy consumption, and a multi-objective optimization was conducted to analyze the relationship between these two. Here, we define the throughput:

$$Throughput = \frac{\sum_{i=1}^{N_{Comp}} Feed_i}{t_{cy}(L_1 + L_2)} \tag{22}$$

The objective function for process optimization is formulated as follows.

$$\max_u Throughput - M\epsilon_1 - M\epsilon_2 \tag{23}$$

where *Feed* [mol/m²] is the total molar volume of gas that enters the VPSA; t_{cy} [s] is the cycle time; L_1 and L_2 [m] are the height of column1 and column2; ϵ_1 and $\epsilon_2 [-]$ are tolerance variables to enforce a cyclic steady state for column 1 and 2, respectively; M is the penalty constant set to 5000; u is a vector of decision variables. The definition of u is discussed below. This objective function maximizes the throughput while penalizing the deviations from the cyclic steady state (CSS); the deviations from the CSS for Columns 1 and 2 are bounded by ϵ_1 and ϵ_2 , respectively, which are forced to be sufficiently close to zero at the optimal solution, as discussed below.

The purity and recovery of component i are defined as follows:

$$Purity_i = \frac{\sum_{k \in S_i} \int_{t_k}^{t_{k+1}} y_i|_{z=L} dt}{\sum_{k \in S_i} \int_{t_k}^{t_{k+1}} y_i|_{z=L} dt} \tag{24}$$

$$Recovery_i = \frac{\sum_{k \in S_i} \int_{t_k}^{t_{k+1}} y_i|_{z=L} dt}{\int_0^{t_{cycle}} y_{Feed,i} dt} \tag{25}$$

where $y_{feed,i}$ is the mole fraction of component i , and the set S_i is given as follows: $S_{H_2} = \{2, 3\}$, $S_{N_2} = \{4, 5\}$, and $S_{CO_2} = \{6, 7\}$ Using these definition, the following constraints are implemented:

$$Purity_i \geq Pur_{min,i} \tag{26}$$

$$Recovery_i \geq Rec_{min,i} \tag{27}$$

$$E \leq E_{max} \tag{28}$$

where $i = H_2, CO_2$; $Pur_{min,i}$ and $Rec_{min,i}$ are the lower bound of purity and recovery of component i , respectively; E [kJ/mol] is the energy consumption for a unit mole of recovered gas; E_{max} is the upper bound of energy consumption. The energy consumption E is given by:

$$E = \frac{work_{ad} + work_{de}}{Product} \tag{29}$$

where *Product* [mol] is the total molar volume of recovered CO₂ and H₂; and $work_{ad}$ and $work_{de}$ [kJ] are the work of adsorption and desorption step given by the following equations;

$$work_{ad} = \begin{cases} \frac{298.15\gamma R}{\gamma - 1} \pi R_b^2 \int_0^{t_2} \frac{1}{\eta_{blower}} \left(\frac{P(t)}{P_{atm}}^{\frac{\gamma-1}{\gamma}} - 1 \right) \frac{uP}{RT} dt & \text{if } P(t) \geq P_{atm} \\ 0 & \text{if } P(t) < P_{atm} \end{cases} \tag{30}$$

$$work_{de} = \frac{298.15\gamma R}{\gamma - 1} \pi R_b^2 \int_{t_4}^{t_7} \frac{1}{\eta_{pump}} \left(\frac{P_{bl}}{P(t)}^{\frac{\gamma-1}{\gamma}} - 1 \right) \frac{uP}{RT} dt \tag{31}$$

where, η_{blower} and $\eta_{pump} [-]$ are the efficiency of blower and pump, with $\eta_{blower} = 0.8$; P_{bl} is the pressure at the end of blowdown step; P_{atm} [kPa] is the atmospheric pressure; $\gamma [-]$ is the heat capacity ratio; and η_{pump} is the efficiency of the vacuum pump modeled by the following quadratic function:

$$\eta_{pump} = -9.5 \times 10^{-5} \left(\frac{P(t)|_{z=L}}{1000} \right)^2 + 9.632 \times 10^{-3} \left(\frac{P(t)|_{z=L}}{1000} \right) + 9.494 \times 10^{-3} \quad (32)$$

where L represents the outlet of each column. The pump efficiency was calculated from the characteristic curves of an industrial vacuum pump (TRM1253, Unozawa-gumi Iron Works, Ltd, Japan), which is plotted in Fig. 4. There exists a maximum at around 50 kPa.

In the optimization, the boundary condition of outlet pressure is dependent on the decision variables, which can be different from the one used in the experiments. In this study, the pressure profiles are parameterized as shown in Fig. 5. In addition to the operations shown in Fig. 2, we assumed and modeled a process called desorption IV, in the period from t_6 to t_7 , in which the vacuum pump pulls out Product from column 1 at constant pressure. The molar flux for this step is calculated using the same formula as $Product_i$ in Table S1. In the following, the end time of the pressurization, the adsorption, the blowdown, and the desorption I-IV are denoted as $t_1, t_2, t_3, t_4, t_5, t_6$, and t_7 , respectively.

The outlet pressure for Column 1 is assumed to follow the following equation:

$$P_1|_{z=L_1} = \begin{cases} \alpha_{pr}t + P_{de} \text{ pressurization } t_0 \leq t \leq t_1 \\ P_{ad} \text{ adsorption } t_1 \leq t \leq t_2 \\ \alpha_{bl}(t - t_2) + P_{ad} \text{ blowdown } t_2 \leq t \leq t_3 \\ P_{bl} \text{ desorption I } t_3 \leq t \leq t_4 \\ \left(\sum_{i=1}^2 \gamma_i e^{-\delta_i(t-t_4)} + P_{final} \right) \times 1.01 \times 10^3 \text{ desorption II } t_4 \leq t \leq t_5 \\ \left(\sum_{i=1}^2 \gamma_i e^{-\delta_i(t-t_4)} + P_{final} \right) \times 1.01 \times 10^3 \text{ desorption III } t_5 \leq t \leq t_6 \\ P_{de} \text{ desorption IV } t_6 \leq t \leq t_7 \end{cases} \quad (33)$$

where P_{final} is set to 2.0 kPa. Similarly, the outlet pressure for Column 2 is assumed to follow the following equation:

$$P_2|_{z=L_2} = \begin{cases} \alpha_{pr}t + P_{de} \text{ pressurization } t_0 \leq t \leq t_1 \\ P_{ad} \text{ adsorption } t_1 \leq t \leq t_2 \\ \alpha_{bl}(t - t_2) + P_{ad} \text{ blowdown } t_2 \leq t \leq t_3 \\ \alpha_{de}(t - t_3) + P_{bl} \text{ desorption I } t_3 \leq t \leq t_4 \\ P_{de} \text{ desorption II, III, IV } t_4 \leq t \leq t_7 \end{cases} \quad (34)$$

The coefficients in the linear equations in Eqs. (33) and (34) are determined as follows: the pressure is assumed to change linearly in pressurization ($\alpha_{pr}t + P_{de}$) and blowdown

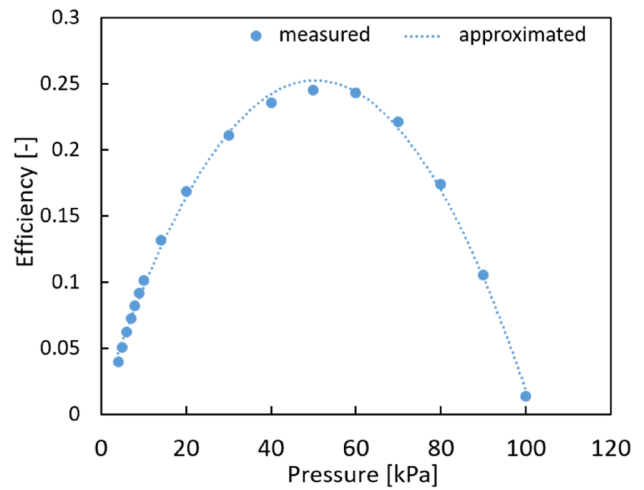


Fig. 4 Pump efficiency modeling

($\alpha_{bl}(t - t_2) + P_{ad}$) for column 1, and pressurization ($\alpha_{pr}t + P_{de}$), blowdown ($\alpha_{bl}(t - t_2) + P_{ad}$), and desorption I ($\alpha_{de}(t - t_3) + P_{bl}$) for column 2. In these equations, the coefficients α_{pr} and α_{bl} were set referring to the experimental conditions: $\alpha_{pr} = (P_{ad} - P_{de})/t_1 = (152 - 5)/30 = 4.9$ 0 kPa/s, $\alpha_{bl} = (P_{bl} - P_{ad})/t_3 = (140 - 152)/1.1 = -10.9$ kPa/s.

By fixing these rates of pressure increase and decrease, we avoid unrealistic operations of rapid pressure change. We found that accurate fitting of the pressure is critical; our attempts of using conventional valve equations tend to show substantial deviations from the experimental pressure measurements. This is partly because of the delay in valve actions which cannot be ignored in the timescale of our modeling. It is assumed that this process can be scaled up without changing the bed heights, while increasing the column diameter; thus the pressure changes remain the same in scaled-up processes [53].

Finally, the pressure for desorption II and III in column 1 are given by exponential functions which works well

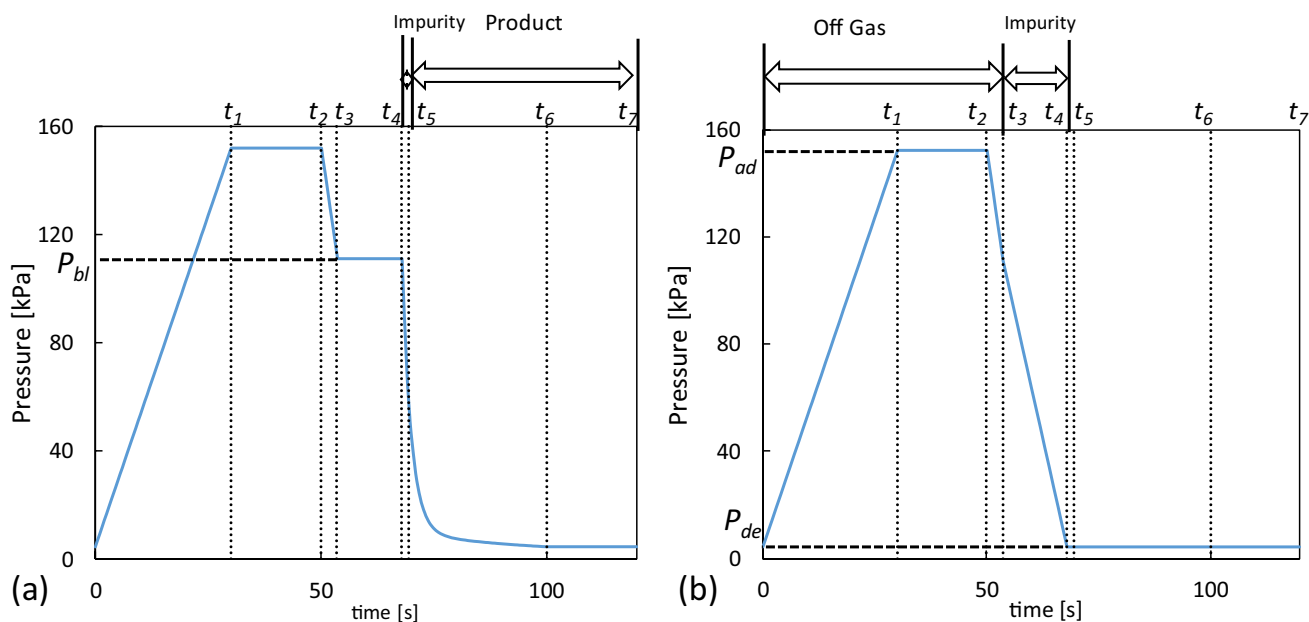


Fig. 5 Outlet column pressure for optimization; **a** Column 1; and **b** Column 2

for extrapolation, as opposed to polynomials in Eqs. (12) and (13). The exponential function represents our experimental observation well, where further pressure change cannot be achieved near the end of the desorption step. The coefficients γ_i and δ_i were determined according to the experimental pressure measurements as shown in Table S4 in the Supporting Information.

Table 3a and b shows the decision variables and optimization constraints, respectively. There are eight decision variables in total. Here, P_{ad} [kPa] is the pressure in the adsorption step; and F [NL/min] is the feed inflow rate. The time intervals, $t_i - t_{i-1}$ for $i=2, 5, 6,$ and $7,$ are implemented as

decision variables. The initial values, except for t_6-t_5 and $t_7-t_6,$ are from the experimental operating conditions. Since desorption IV was not present in the experiment, a lower limit of 1 s was set for $t_7-t_6,$ and this lower limit was used as the initial value. The initial value was obtained for t_6 by subtracting one second of t_7-t_6 from the t_6-t_5 in the experimental condition. Furthermore, $t_4-t_3,$ the time for desorption I, which is short and found to be relatively insensitive, is set to a fixed value. It should be noted that some of the variables are correlated and have similar influences to the performance indicators; for example, when the column length is shortened, the performance indicators changes similarly to the

Table 3 Optimization conditions

(a) Decision variables			
Variable	Lower bound	Upper bound	Initial value
P_{ad} [kPa]	130	1,000	152
t_2-t_1 [s]	1.00	1,000	30.0
t_5-t_4 [s]	1.0×10^{-5}	1,000	1.70
t_6-t_5 [s]	1.00	1,000	31.9
t_7-t_6 [s]	1.00	1,000	1.00
F [NL/min]	1.00	31.2	3.12
L_1 [m]	0.01	2.00	0.06
L_2 [m]	0.01	2.00	0.2
(b) Bounds in constraints			
Variable	Lower bound	Upper bound	
ϵ_1 [-]	0	0.1	
ϵ_2 [-]	0	0.1	
ad_{ratio} [-]	0.9	1.1	

case where the feed flow rates is increased. Such correlations could be analyzed only heuristically. In this work, instead of relying on heuristic decisions, we include many variables as decision variables, and attempt to find the optimal solution numerically.

Some of the time variables, t_1, t_3-t_2, t_4-t_3 , as well as the desorption pressure P_{de} are determined as dependent variables from the decision variables shown in Table 3. For example, t_1 is given by Eq. (33) as $P_{ad} = \alpha_{ad}t_1 + P_{de}$, where the blow-down pressure P_{bl} is set to 111 kPa. Similarly, t_3-t_2 is given by Eq. (34) as $P_{bl} = \alpha_{bl}(t_3 - t_2) + P_{ad}$. Finally, the desorption pressure is also given by Eq. (33) as a function of the decision variable t_4 and t_6 :

$$P_{de} = \left(\sum_{i=1}^2 \gamma_i e^{-\delta_i(t_6-t_4)} + P_{final} \right) \times 1.01 \times 10^3 \quad (35)$$

We also consider a constraint to assure continuous processing of the feed gas using only two VPSA units, each of which consists only of a single column. The feed gas can be supplied only during the adsorption steps represented by t_2 , but not during the desorption steps represented by t_7-t_2 . Here, we define ad_{ratio} [–] as the ratio of the t_2 to the subtraction of the t_2 , and t_7 .

$$ad_{ratio} = \frac{t_2}{t_7 - t_2} \quad (36)$$

We require that ad_{ratio} must be sufficiently close to 1.

Table 4 Experimental values and model fitting of purity and recovery

	Purity _{CO2}	Recovery _{CO2}	Purity _{H2}	Recovery _{H2}
Experiment [%]	89.4	71.8	53.4	75.2
Model [%]	83.7	75.7	51.6	72.4

Cyclic Steady State (CSS) constraints must be enforced for the optimization of cyclic adsorption processes. CSS is a state that the column profile at the start of the cycle is the same as those at the end. CSS is defined by Eq. (37).

$$\varphi(z, t)|_{t=0} - \varphi(z, t)|_{t=t_{cy}} = 0 \quad (37)$$

where φ is a vector of state variables, $\varphi = [y_i, q_i, T, T_{wall}]^T$. The above equation is approximated using small positive values of ε_1 and ε_2 ,

$$-\varepsilon_1 \leq \varphi_1(z, t)|_{t=0} - \varphi_1(z, t)|_{t=t_{cy}} \leq \varepsilon_1 \quad (38)$$

$$-\varepsilon_2 \leq \varphi_2(z, t)|_{t=0} - \varphi_2(z, t)|_{t=t_{cy}} \leq \varepsilon_2, \quad (39)$$

where φ_1 and φ_2 are state variables for Columns 1 and 2, respectively. In the above two constraints, the state variables for Columns 1 and 2 are enforced to be within the tolerances $\pm\varepsilon_1$ and $\pm\varepsilon_2$, respectively, which converge toward zero by the penalty terms in the objective function in Eq. (23) with the upper and lower bounds in Table 3b.

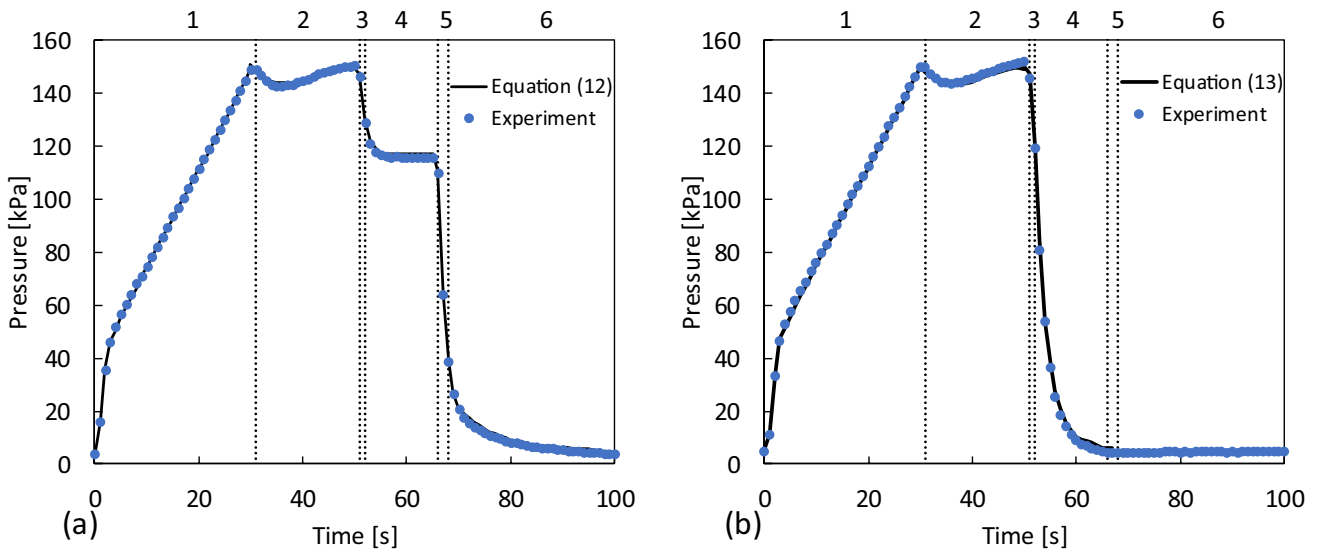


Fig. 6 Outlet pressure at the column outlet; **a** Column 1; and **b** Column 2. The numbers in the figure indicate, respectively, 1 for the pressurization, 2 for the adsorption, 3 for the blowdown, 4 for the desorption I, 5 for the desorption II, and 6 for the desorption III

4 Results and discussion

4.1 Model fitting

4.1.1 Fitting the outlet pressure to the experimental conditions

Figure 6 shows the pressure boundary conditions for the simulation, Eqs. (12) and (13), and the pressure measurements from the experiment. The coefficients in these equations for column 1 and column 2 were determined by fitting these equations to the experimental measurements (Table S5 and S6 in Supporting Information). Due to the delay in the valve actions, the pressure in Column 1 keeps decreasing even at the beginning of Step 4, Desorption I. If the column height must be scaled up, the blowdown time may need to be increased due to pressure drop increase [53].

4.1.2 Process model fitting

Table 4 shows the model fitting for the experiment. It can be seen that both the purity and recovery of CO₂ have errors of up to 6%, while those of H₂ are up to 3%. While reducing the value of ρ in Eq. (21) further would allow the parameter values to deviate from literature and reduce the model error, overfitting and parameter values that are physically inconsistent must be avoided. Also, Table 5 shows the estimated parameters and literature value used as the initial value of the estimation. The initial values of K_1 and K_2 are taken from

previous studies and fitted into Eq. (8) [54, 55], while those for De are from Shigaki et al. [41].

Figure 7 shows the fitting and validation results, confirming the improvement of the estimated parameters (circles) from the initial parameters (crosses). The model was fitted to a single experimental data shown by the empty symbols. The resulting model was validated against new data sets shown by the closed symbols. In particular, the deviations of N₂ (green) are resolved in Off Gas (Fig. 7a), as well as in Impurity (Fig. 7b). We also note that some minor deviations of CO₂ (blue) remain even after parameter estimation.

There are two potential approaches to further improve the predictions given by the estimated parameters. The first is to change the adsorption isotherm model. The Langmuir-type isotherm, which is relatively simple, can be replaced by another model with a larger number of parameters such as the bi-Langmuir or Langmuir–Freundlich. The second is the modeling of the dead volume; the model developed in this study is only for the adsorption column, and ignores the volume of the pipes, pump and back pressure valve. Mixing in such dead volume may be modeled by a stirred tank model [50].

Information such as the time variation of mole fractions at the column outlets, which cannot be measured experimentally, can be estimated using the obtained model. Figure 8 shows the time variation of the mole fraction at the column outlet. The graph shows that the enrichment of H₂ is achieved because most of the CO₂ is removed in column 1 and the separation of N₂ and H₂ occurs in column 2. Looking at the region from 0 to 10 s in Fig. 8a, we can see that breakthrough of H₂ occurs early, which is followed by that

Table 5 Estimated parameters and initial values

i	K_{1i} [bar ⁻¹]		K_{2i} [K]		De [m ² /s]	
	Estimated	Initial value	Estimated	Initial value	Estimated	Initial value
N ₂	4.55×10^{-3}	6.00×10^{-3}	3.57	2.20	2.36×10^{-7}	2.05×10^{-7}
CO ₂	6.37×10^{-1}	4.32×10^{-1}	4.39	1.72	6.83×10^{-8}	2.05×10^{-7}
H ₂	1.26×10^{-4}	8.70×10^{-5}	4.80×10^{-1}	1.13	6.83×10^{-8}	2.05×10^{-7}

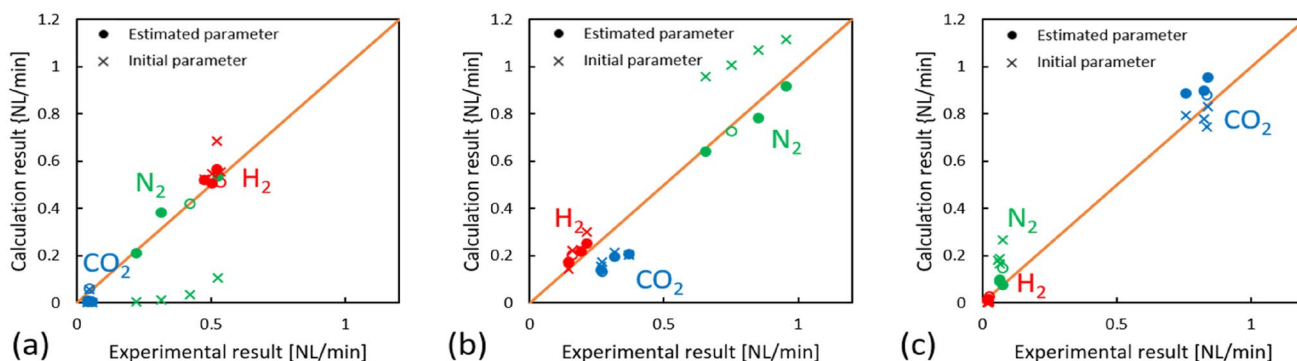


Fig. 7 Model validation (prediction) for gas flow rates; **a** off gas **b** impurity gas **c** product gas. The red, blue, green plots show H₂, CO₂, and N₂, respectively. Open symbols show the data used for fitting, and closed ones show the validation results (Color figure online)

Fig. 8 Mole fractions at the outlet of **a** column 1; and **b** column 2 (Color figure online)

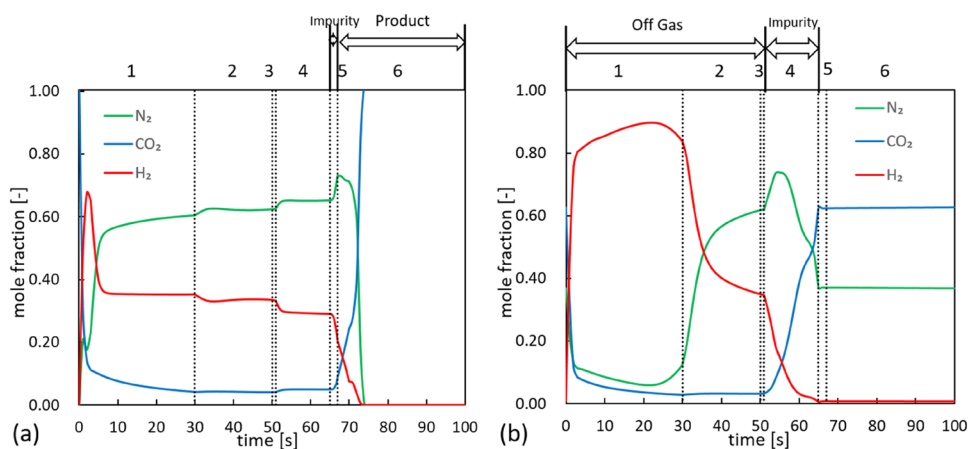


Table 6 Comparison of experimental and optimized performance

	Experiment	Optimization		Experiment	Optimization
Energy Consumption [kJ/mol]	93.8	65.5	Throughput [mol/m ³ /s], maximized	3.06	3.48
$Purity_{CO_2}$ [%]	89.4	95.7	$Recovery_{CO_2}$	71.8	76.2
$Purity_{H_2}$ [%]	53.4	53.4*	$Recovery_{H_2}$	75.2	75.2*

The optimization was performed with the following conditions to match the experimental results: $Pur_{min,CO_2}=89.4\%$, $Rec_{min,CO_2}=71.8\%$, $Pur_{min,H_2}=53.4\%$, $Rec_{min,H_2}=75.2\%$. Values shown with asterisks (*) show the values at the lower bounds

of N_2 . On the other hand, it can be confirmed that the CO_2 concentration is always low until 50 s when the adsorption process ends. This indicates that most of the influx into column 2 during the pressurization and adsorption steps is H_2 and N_2 . In addition, looking at the region of 0 to 40 s of (b), the timings of the breakthroughs of H_2 and N_2 are sufficiently apart, confirming that H_2 is enriched. It can also be seen that the mole fraction of N_2 is higher at the end of the cycle in Fig. 8b than in Fig. 8a, confirming N_2 is further enriched in Column 2.

One of the advantages of splitting the column into two columns is lower energy consumption, which can also be seen from Fig. 8. Purified CO_2 is collected from the outlet of Column 1 (right end of Fig. 8a), where CO_2 is highly purified. There, CO_2 , which has a high affinity towards the adsorbent, is removed effectively by the vacuum pump from the middle of the bed. This operation, where the strongly adsorbing component is pulled out from the middle of the bed, avoids incurring pressure drop across the entire bed length, lowering the energy consumption of the vacuum pump.

4.2 Optimization results

4.2.1 Comparison of experiment and optimization

To compare with experimental and optimized performance, optimization was conducted constraining the purity,

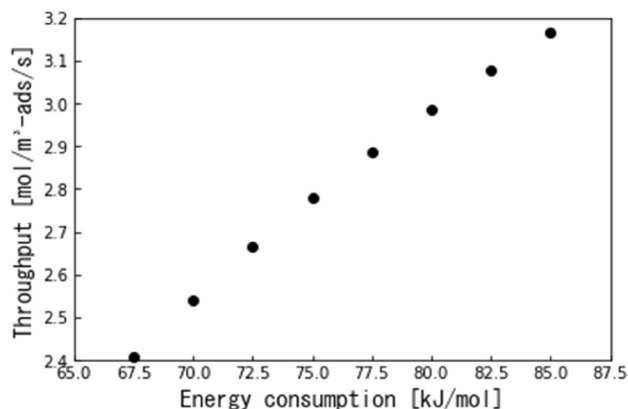


Fig. 9 Pareto optimal solutions for energy consumption and throughput with $Pur_{min,CO_2}=99\%$, $Rec_{min,CO_2}=90\%$, $Pur_{min,H_2}=60\%$, $Rec_{min,H_2}=65\%$

recovery, energy consumption to Pur_{min} , Rec_{min} , and E_{max} at the same values from the experiments, respectively, (Table 6). Comparing the experimental and optimized performance in Table 6, it is confirmed that the optimization finds better operating conditions; the throughput increases by approximately 14%, while reducing the energy consumption by approximately 30% at the same purity and recovery of H_2 . In addition, CO_2 purity and recovery at the optimal solution are 6% and 4% higher than those from the experiment, respectively. This improvement is expected because

the optimal solution employs a higher desorption pressure of P_{de} from that of the experimental condition, 5.71 vs. 5.10 kPa, to reduce the energy consumption, while the length of the second column L_2 is longer at the optimal solution, 0.41 vs. 0.20 m, to maintain the required purity and recovery. Further details are given in Table S7 in the Supporting Information. It should be noted that this prediction may be subject to the assumptions of the pump efficiency discussed in Sect. 3.4.

4.2.2 Pareto optimization

To analyze relationship of performance index of the process, optimization whose $Pur_{minCO_2}=99\%$, $Rec_{minCO_2}=90\%$, $Pur_{minH_2}=60\%$ and $Rec_{minH_2}=65\%$ was conducted while varying E_{max} from 67.5 kJ/mol to 85 kJ/mol. Figure 9 shows the optimization results, showing the trade-off between throughput and energy consumption for a unit mole of recovered CO_2 and H_2 . In all of the optimal solutions, the inequality constraints shown in Eqs. (26) and (27) are active; i.e. they are exactly at the lower bounds. It should be noted that concentrating the dilute H_2 in our case study is very challenging, where the H_2 concentration in the feed is as low as 23%; this value is significantly lower than that in Streb and Mazzotti (2019), 50%.

4.2.3 Decision variables

Figure 10a shows the relationship between the adsorption pressure, or the target pressure reached at the end of the adsorption step, versus the energy utilization, and (b) shows the relationship between the desorption pressure, or the target pressure at the end of the desorption step versus the energy utilization. It can be found that when the energy utilization is highly constrained, energy consumption for the vacuum pump should be reduced while that for the compressor can be sacrificed; from Fig. 10a, it can be found that the

adsorption pressure is higher at lower energy consumption, which should be reduced when higher energy consumption is tolerated. Similarly, Fig. 7b shows that the desorption pressure is higher at lower energy consumption, which should be decreased when higher energy consumption is tolerated. The desorption pressure, which varied from 3.0 to 4.4 kPa, are dependent on the efficiencies of the compressor and vacuum pump. If a too low pressure must be avoided, the upper bound of the desorption times, t_7-t_6 and t_6-t_5 , should be shortened, so that depressurization is completed before reaching a too low pressure.

In this study, the optimal adsorption pressure is significantly higher than atmospheric pressure, which is contrary to the conventional approaches to save energy [56]. This is because the VPSA in this study is intended to capture two components, the second column requires high pressure to separate N_2 and H_2 , which adsorbs weakly. It should also be noted that the above finding may highly depend on the assumptions of the efficiency of the compressor and vacuum pump. As introduced in Chapter 3, the efficiency of a

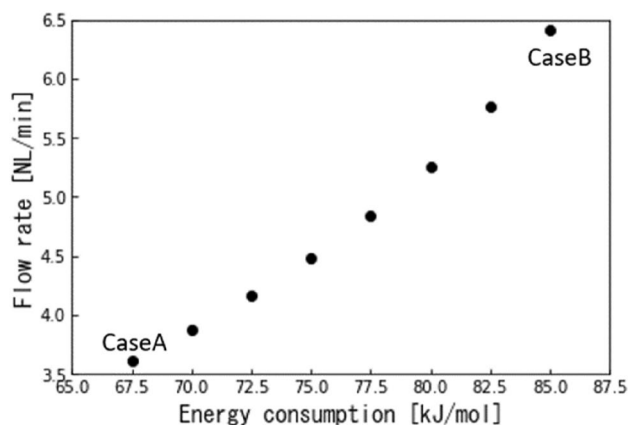


Fig. 11 Energy consumption and feed flow rate

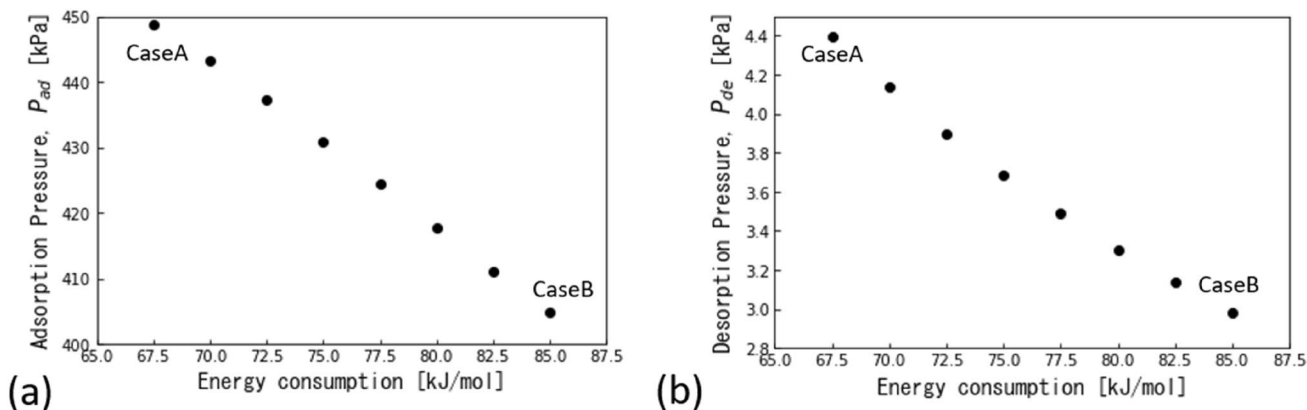


Fig. 10 Optimal operating pressures; a Adsorption pressure and energy consumption; and b desorption pressure and energy consumption

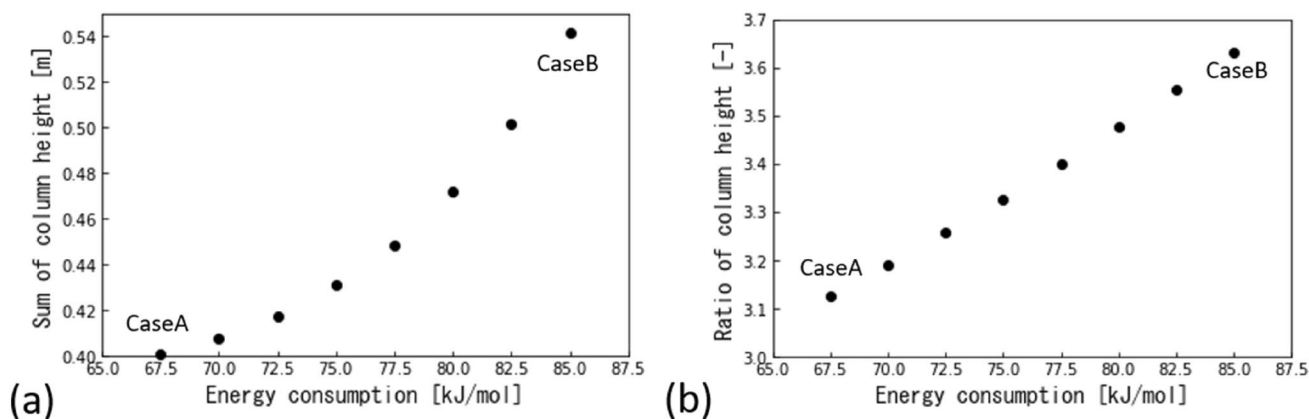


Fig. 12 Energy consumption and optimal column height; **a** the sum of the heights of the two columns; **b** the height ratio of Column 2

vacuum pump is measured and given as a function of pressure. In contrast, the efficiency of the compressor is given as a constant.

Figure 11 shows the relationship between the energy consumption and the flow rate of the feed gas at the entrance of column 1, which confirms that the feed gas flow rate can be increased to achieve higher productivity as higher energy consumption is tolerated. The increase in the feed gas flow rate shortens the adsorption time, which leads to a shorter desorption time as required by the constraint in Eq. (36). Due to this constraint, desorption must be completed in a short time at a lower pressure and higher feed gas flow rate, requiring higher energy consumption of the vacuum pump.

Figure 12a shows the sum of the heights of the two columns increases when higher energy consumption is tolerated. An increase in column height leads to an increase in pressure drop, which in turn increases energy consumption. The longer column facilitates meeting the purity and recovery constraints, allowing higher feed gas flow rates to increase the productivity.

Figure 12b shows the height ratio of Column2 also increases when higher energy consumption is tolerated. This is because enrichment of H_2 is more difficult than that of CO_2 ; while CO_2 can be concentrated by extending the time of desorption II, the only way to concentrate H_2 is to remove N_2 by adsorption in column 2. As the feed gas flow rate increases to achieve higher throughput, the amount of N_2 to be removed also increases. To cope with this difficulty, the amount of adsorbent must be increased to achieve sufficient separation performance. It is confirmed in Fig. 11 that the feed gas flow rate increases as the energy consumption increases.

The optimizations were performed by varying the energy consumption, which allows us to analyze the relationship between the throughput and energy consumption. Such an analysis will enable us to select the optimum operating conditions for multiple scenarios pursuing reduction of capital

cost (i.e., higher throughput), versus pursuing reduction of operating cost (i.e. lower energy consumption). On the other hand, there is still an error between the values given by the model and experiments under the same conditions, as can be seen in Table 4 and Fig. 7. Further experimental and modeling effort, especially, improving the multi-component isotherms, may be necessary to validate the model.

5 Conclusions

In this study, we proposed a new VPSA process for simultaneous separation of CO_2 and H_2 from BFG. This process utilizes two columns in series and a gas fraction line downstream of the columns to achieve high separation performance for CO_2 and H_2 . In addition, the proposed operation that require only two columns reduces equipment cost from that of conventional VPSAs for simultaneous separation of multiple components. In addition, a pilot-scale experiment was conducted to verify the performance of this process. A model-based analysis was also carried out utilizing the pilot-scale experimental data. A mathematical model of the process was first developed to enable prediction of the operation results by calculation. In addition, the adsorption isotherm parameters and mass transfer coefficients were estimated by fitting the model to the experimental data. The resulting model predicted flow rates of all gases within an error of 6%. The obtained model and parameters allow us to estimate gas compositions and concentrations that were not measured experimentally. Using the model, optimization was performed to maximize the throughput, which confirms potential improvement from the design employed in our experiment. Furthermore, multi-objective optimization revealed a Pareto set for the trade-off between energy consumption and throughput under the purity and recovery constraints, identifying the optimal design and operating conditions

such as operating pressure, step times, feed gas flow rate, and column height.

Future research could include improvement of the model and optimization. Modeling the multi-component adsorption isotherm can be improved by using different adsorption isotherms, and the dead volume may need to be included in the model. In the optimization, sensitivities with respect to the purity and recovery constraints should also be analyzed, and alternative operating strategies, including reflux operations, should be investigated. Finally, variations in the feed compositions should be handled by changing the decision variables to maintain the product purity and recovery, which may be aided by an automatic control scheme [57].

Supplementary Information The online version contains supplementary material available at <https://doi.org/10.1007/s10450-022-00371-x>.

Acknowledgements This article is based on results obtained from a project, JPNP16002, commissioned by the New Energy and Industrial Technology Development Organization (NEDO).

Funding Funding was provided by New Energy and Industrial Technology Development Organization (Grant Number JPNP16002).

Declarations

Conflict of interest The authors declare that they have no known competing financial interests or personal relationships that could have appeared to influence the work reported in this paper.

References

- Houghton, J.: Global warming. *Rep. Prog. Phys.* **68**(6), 1343–1403 (2005). <https://doi.org/10.1088/0034-4885/68/6/R02>
- Smit, B., Reimer, J., Oldenburg, C., Bourg, I.: *Introduction to Carbon Capture and Sequestration*. Imperial College Press, London (2014)
- Tapia, J.F.D., Lee, J.-Y., Ooi, R.E.H., Foo, D.C.Y., Tan, R.R.: A review of optimization and decision-making models for the planning of CO₂ capture, utilization and storage (CCUS) systems. *Sustain. Prod. Consump.* **13**, 1–15 (2018). <https://doi.org/10.1016/j.spc.2017.10.001>
- International Energy Agency. *Energy technology perspectives*. In: *Strategies* (Issue June), Paris (2008)
- Haraoka, T., Mogi, Y., Saima, H.: PSA system for the recovery of carbon dioxide from blast furnace gas in steel works the influence of operation conditions on CO₂ separation. *Kagaku Kogaku Ronbunshu* **39**(5), 439–444 (2013). <https://doi.org/10.1252/kakoronbunshu.39.439>
- National Institute for Environmental Studies. *National Greenhouse Gas Inventory Report of JAPAN 2020* (2020)
- Shigaki, N., Mogi, Y., Haraoka, T., Sumi, I.: Reduction of electric power consumption in CO₂-PSA with zeolite 13X adsorbent. *Energies* **11**(4), 900 (2018). <https://doi.org/10.3390/en11040900>
- Chen, W.H., Chen, C.Y.: Water gas shift reaction for hydrogen production and carbon dioxide capture: a review. *Appl. Energy* **258**(2019), 114078 (2020). <https://doi.org/10.1016/j.apenergy.2019.114078>
- Rhodes, C., Hutchings, G.J., Ward, A.M.: Water-gas shift reaction: finding the mechanistic boundary. *Catal. Today* **23**(1), 43–58 (1995). [https://doi.org/10.1016/0920-5861\(94\)00135-O](https://doi.org/10.1016/0920-5861(94)00135-O)
- Wang, W., Gong, J.: Methanation of carbon dioxide: an overview. *Front. Chem. Eng. China* **5**(1), 2–10 (2011). <https://doi.org/10.1007/s11705-010-0528-3>
- Wang, W.H., Himeda, Y., Muckerman, J.T., Manbeck, G.F., Fujita, E.: CO₂ hydrogenation to formate and methanol as an alternative to photo- and electrochemical CO₂ reduction. *Chem. Rev.* **115**(23), 12936–12973 (2015). <https://doi.org/10.1021/acs.chemrev.5b00197>
- Streb, A., Mazzotti, M.: Novel adsorption process for co-production of hydrogen and CO₂ from a multicomponent stream-part 2: application to steam methane reforming and autothermal reforming gases. *Ind. Eng. Chem. Res.* **59**(21), 10093–10109 (2020). <https://doi.org/10.1021/acs.iecr.9b06953>
- Haghpanah, R., Majumder, A., Nilam, R., Rajendran, A., Farooq, S., Karimi, I.A., Amanullah, M.: Multiobjective optimization of a four-step adsorption process for postcombustion CO₂ capture via finite volume simulation. *Ind. Eng. Chem. Res.* **52**(11), 4249–4265 (2013). <https://doi.org/10.1021/ie302658y>
- Haghpanah, R., Nilam, R., Rajendran, A., Farooq, S., Karimi, I.A.: Cycle synthesis and optimization of a VSA process for post-combustion CO₂ capture. *AIChE J.* **59**(12), 4735–4748 (2013). <https://doi.org/10.1002/aic.14192>
- Farooq, S., Ruthven, D.M.: Numerical simulation of a kinetically controlled pressure swing adsorption bulk separation process based on a diffusion model. *Chem. Eng. Sci.* **46**(9), 2213–2224 (1991). [https://doi.org/10.1016/0009-2509\(91\)85121-D](https://doi.org/10.1016/0009-2509(91)85121-D)
- Malek, A., Farooq, S.: Hydrogen purification from refinery fuel gas by pressure swing adsorption. *AIChE J.* **44**(9), 1985–1992 (1998). <https://doi.org/10.1002/aic.690440906>
- Saima, H., Mogi, Y., Haraoka, T.: Development of PSA system for the recovery of carbon dioxide and carbon monoxide from blast furnace gas in steel works. *Energy Procedia* **37**(19), 7152–7159 (2013). <https://doi.org/10.1016/j.egypro.2013.06.652>
- Susarla, N., Haghpanah, R., Karimi, I.A., Farooq, S., Rajendran, A., Tan, L.S.C., Lim, J.S.T.: Energy and cost estimates for capturing CO₂ from a dry flue gas using pressure/vacuum swing adsorption. *Chem. Eng. Res. Des.* **102**, 354–367 (2015). <https://doi.org/10.1016/j.cherd.2015.06.033>
- Hasan, M.M.F., First, E.L., Boukouvala, F., Floudas, C.A.: A multi-scale framework for CO₂ capture, utilization, and sequestration: CCUS and CCU. *Comput. Chem. Eng.* **81**, 2–21 (2015). <https://doi.org/10.1016/j.compchemeng.2015.04.034>
- Agarwal, A., Biegler, L.T., Zitney, S.E.: A superstructure-based optimal synthesis of PSA cycles for post-combustion CO₂ capture. *AIChE J.* **56**(7), 1813–1828 (2010). <https://doi.org/10.1002/aic.12107>
- Casas, N., Schell, J., Joss, L., Mazzotti, M.: A parametric study of a PSA process for pre-combustion CO₂ capture. *Sep. Purif. Technol.* **104**, 183–192 (2013). <https://doi.org/10.1016/j.seppur.2012.11.018>
- Leperi, K.T., Yancy-Caballero, D., Snurr, R.Q., You, F.: 110th anniversary: surrogate models based on artificial neural networks to simulate and optimize pressure swing adsorption cycles for CO₂ capture. *Ind. Eng. Chem. Res.* **58**(39), 18241–18252 (2019). <https://doi.org/10.1021/acs.iecr.9b02383>
- Ruthven, D.M., Farooq, S., Knaebel, K.S.: *Pressure Swing Adsorption*. Wiley, New York (1994)
- Ko, D., Siriwardane, R., Biegler, L.T.: Optimization of pressure swing adsorption and fractionated vacuum pressure swing adsorption processes for CO₂ capture. *Ind. Eng. Chem. Res.* **44**(21), 8084–8094 (2005). <https://doi.org/10.1021/ie050012z>
- Ho, M.T., Allinson, G.W., Wiley, D.E.: Reducing the cost of CO₂ capture from flue gases using pressure swing adsorption. *Ind. Eng.*

- Chem. Res. **47**(14), 4883–4890 (2008). <https://doi.org/10.1021/ie070831e>
26. Xiao, P., Zhang, J., Webley, P., Li, G., Singh, R., Todd, R.: Capture of CO₂ from flue gas streams with zeolite 13X by vacuum-pressure swing adsorption. *Adsorption* **14**(4–5), 575–582 (2008). <https://doi.org/10.1007/s10450-008-9128-7>
 27. Grande, C.A.: Advances in pressure swing adsorption for gas separation. *ISRN Chem Eng* **2012**, 1–13 (2012). <https://doi.org/10.5402/2012/982934>
 28. Choi, W.K., Kwon, T.I., Yeo, Y.K., Lee, H., Song, H.K., Na, B.K.: Optimal operation of the pressure swing adsorption (PSA) process for CO₂ recovery. *Korean J. Chem. Eng.* **20**(4), 617–623 (2003). <https://doi.org/10.1007/BF02706897>
 29. Na, B.K., Lee, H., Koo, K.K., Song, H.K.: Effect of rinse and recycle methods on the pressure swing adsorption process to recover CO₂ from power plant flue gas using activated carbon. *Ind. Eng. Chem. Res.* **41**(22), 5498–5503 (2002). <https://doi.org/10.1021/ie0109509>
 30. Kim, Y.J., Nam, Y.S., Kang, Y.T.: Study on a numerical model and PSA (pressure swing adsorption) process experiment for CH₄/CO₂ separation from biogas. *Energy* **91**, 732–741 (2015). <https://doi.org/10.1016/j.energy.2015.08.086>
 31. Wang, L., Liu, Z., Li, P., Yu, J., Rodrigues, A.E.: Experimental and modeling investigation on post-combustion carbon dioxide capture using zeolite 13X-APG by hybrid VTSA process. *Chem. Eng. J.* **197**, 151–161 (2012). <https://doi.org/10.1016/j.cej.2012.05.017>
 32. Abdeljaoued, A., Relvas, F., Mendes, A., Chahbani, M.H.: Simulation and experimental results of a PSA process for production of hydrogen used in fuel cells. *J. Environ. Chem. Eng.* **6**(1), 338–355 (2018). <https://doi.org/10.1016/j.jece.2017.12.010>
 33. Hasan, M.M.F., Baliban, R.C., Elia, J.A., Floudas, C.A.: Modeling, simulation, and optimization of postcombustion CO₂ capture for variable feed concentration and flow rate. 1. Chemical absorption and membrane processes. *Ind. Eng. Chem. Res.* **51**(48), 15642–15664 (2012). <https://doi.org/10.1021/ie301571d>
 34. Reynolds, S.P., Ebner, A.D., Ritter, J.A.: New pressure swing adsorption cycles for carbon dioxide sequestration. *Adsorption* **11**(S1), 531–536 (2005). <https://doi.org/10.1007/s10450-005-5980-x>
 35. Sircar, S.: Recent trends in pressure swing adsorption: production of multiple products from a multicomponent feed gas. *Gas Sep. Purif.* **7**(2), 69–73 (1993). [https://doi.org/10.1016/0950-4214\(93\)85003-E](https://doi.org/10.1016/0950-4214(93)85003-E)
 36. Dong, F., Lou, H., Kodama, A., Goto, M., Hirose, T.: A new concept in the design of pressure-swing adsorption processes for multicomponent gas mixtures. *Ind. Eng. Chem. Res.* **38**(1), 233–239 (1999). <https://doi.org/10.1021/ie980323s>
 37. Kumar, R.: Adsorption process for recovering two high purity gas products from multicomponent gas mixtures. Patent No. US-4913709-A (1990).
 38. Sircar, S., Kratz, W.C.: Simultaneous production of hydrogen and carbon dioxide from steam reformer off-gas by pressure swing adsorption. *Sep. Sci. Technol.* **23**(14–15), 2397–2415 (1988). <https://doi.org/10.1080/01496398808058461>
 39. Streb, A., Hefti, M., Gazzani, M., Mazzotti, M.: Novel adsorption process for Co-production of hydrogen and CO₂ from a multicomponent stream. *Ind. Eng. Chem. Res.* **58**(37), 17489–17506 (2019). <https://doi.org/10.1021/acs.iecr.9b02817>
 40. Park, Y., Kang, J.-H., Moon, D.-K., Jo, Y.S., Lee, C.-H.: Parallel and series multi-bed pressure swing adsorption processes for H₂ recovery from a lean hydrogen mixture. *Chem. Eng. J.* **408**, 127299 (2021). <https://doi.org/10.1016/j.cej.2020.127299>
 41. Shigaki, N., Mogi, Y., Kijima, H., Kakiuchi, T., Yajima, T., Kawajiri, Y.: Performance evaluation of gas fraction PSA for CCU process. *Int. J. Greenh. Gas Control* **120**, 103763 (2022)
 42. Ko, D., Siriwardane, R., Biegler, L.T.: Optimization of a pressure-swing adsorption process using zeolite 13X for CO₂ sequestration. *Ind. Eng. Chem. Res.* **42**(2), 339–348 (2003). <https://doi.org/10.1021/ie0204540>
 43. Ko, D., Siriwardane, R., Biegler, L.T.: Optimization of pressure swing adsorption and fractionated vacuum pressure swing adsorption processes for CO₂ sequestration. In: *AIChE Annual Meeting, Conference Proceedings*, November (2004).
 44. Ribeiro, A.M., Grande, C.A., Lopes, F.V., Loureiro, J.M., Rodrigues, A.E.: A parametric study of layered bed PSA for hydrogen purification. *Chem. Eng. Sci.* **63**(21), 5258–5273 (2008). <https://doi.org/10.1016/j.ces.2008.07.017>
 45. Luberti, M., Kim, Y.H., Lee, C.H., Ferrari, M.C., Ahn, H.: New momentum and energy balance equations considering kinetic energy effect for mathematical modelling of a fixed bed adsorption column. *Adsorption* **21**(5), 353–363 (2015). <https://doi.org/10.1007/s10450-015-9675-7>
 46. Japan Stainless Steel Association. Physical properties of stainless steel such as electrical conductivity, magnetic permeability, and thermal expansion (2011). <https://www.jssa.gr.jp/contents/faq-article/q6/>. Accessed 18 June, 2021
 47. Kogakukai, K. (ed.): *Kagaku Kogaku Binran*. Maruzen (2011)
 48. Wen, D., Ding, Y.: Heat transfer of gas flow through a packed bed. *Chem. Eng. Sci.* **61**(11), 3532–3542 (2006). <https://doi.org/10.1016/j.ces.2005.12.027>
 49. Ruthven, D.M.: *Principles of Adsorption and Adsorption Processes*. Wiley, New York (1984)
 50. Suzuki, K., Harada, H., Sato, K., Okada, K., Tsuruta, M., Yajima, T., Kawajiri, Y.: Utilization of operation data for parameter estimation of simulated moving bed chromatography. *J. Adv. Manuf. Process.* **4**(1), 1–18 (2022). <https://doi.org/10.1002/amp.2.10103>
 51. Tie, S., Sreedhar, B., Agrawal, G., Oh, J., Donaldson, M., Frank, T., Schultz, A., Bommarius, A., Kawajiri, Y.: Model-based design and experimental validation of simulated moving bed reactor for production of glycol ether ester. *Chem. Eng. J.* **301**, 188–199 (2016). <https://doi.org/10.1016/j.cej.2016.04.062>
 52. Tie, S., Sreedhar, B., Donaldson, M., Frank, T., Schultz, A.K., Bommarius, A.S., Kawajiri, Y.: Experimental evaluation of simulated moving bed reactor for transesterification reaction synthesis of glycol ether ester. *Adsorption* **25**(4), 795–807 (2019). <https://doi.org/10.1007/s10450-019-00048-y>
 53. Ahn, H., Hong, S.H., Zhang, Y., Lee, C.H.: Experimental and simulation study on CO₂ adsorption dynamics of a zeolite 13X column during blowdown and pressurization: implications of scaleup on CO₂ capture vacuum swing adsorption cycle. *Ind. Eng. Chem. Res.* **59**(13), 6053–6064 (2020)
 54. Shigaki, N., Mogi, Y., Haraoka, T., Furuya, E.: Measurements and calculations of the equilibrium adsorption amounts of CO₂-N₂, CO-N₂, and CO₂-CO mixed gases on 13X zeolite. *SN Appl. Sci.* **2**(3), 1–17 (2020). <https://doi.org/10.1007/s42452-020-2298-y>
 55. Streb, A., Mazzotti, M.: Adsorption in the context of clean hydrogen production: process intensification by integrating H₂ purification and CO₂ capture—a modeling and experimental study of multi-component adsorption. *SSRN Electron. J.* (2021). <https://doi.org/10.2139/ssrn.3811394>
 56. Suzuki, T., Sakoda, A., & Suzuki, M.: The current status and related issues of studies on rapid pressure swing adsorption. *Seisan Kenkyu* **50**(6), 213–220 (1998). <https://doi.org/10.1118/seisankenkyu.50.213>

57. Khajuria, H., Pistikopoulos, E.N.: Dynamic modeling and explicit/multi-parametric MPC control of pressure swing adsorption systems. *J. Process Control* **21**(1), 151–163 (2011). <https://doi.org/10.1016/j.jprocont.2010.10.021>

Publisher's Note Springer Nature remains neutral with regard to jurisdictional claims in published maps and institutional affiliations.

Springer Nature or its licensor (e.g. a society or other partner) holds exclusive rights to this article under a publishing agreement with the author(s) or other rightsholder(s); author self-archiving of the accepted manuscript version of this article is solely governed by the terms of such publishing agreement and applicable law.